remote sensing

MDPI

Article

Climatology of Polar Stratospheric Clouds Derived from CALIPSO and SLIMCAT

Douwang Li [1], Zhe Wang [1], Shun Li [1], Jiankai Zhang [1,*] and Wuhu Feng [2,3]

[1] School of Atmospheric Sciences, Lanzhou University, Lanzhou 730000, China; 220220902911@lzu.edu.cn (D.L.); wangzh2023@lzu.edu.cn (Z.W.); lish2023@lzu.edu.cn (S.L.)
[2] National Centre for Atmospheric Science (NCAS), University of Leeds, Leeds LS2 9PH, UK; w.feng@ncas.ac.uk
[3] Institute for Climate and Atmospheric Science, School of Earth and Environment, University of Leeds, Leeds LS2 9JT, UK
* Correspondence: jkzhang@lzu.edu.cn

Abstract: Polar stratospheric clouds (PSCs) play a crucial role in ozone depletion in the polar stratosphere. In this study, the space-based PSCs record from CALISPO and an offline three-dimensional chemical transport model (SLIMCAT) are used to analyze the PSCs in the Arctic and the Antarctic for the period 2006−2021. Observations indicate that the seasonal evolution of the Antarctic PSC area is similar from year to year. In contrast, the Arctic PSCs show large differences in seasonal variations of coverage and duration in different years. The SLIMCAT simulations effectively capture the seasonal and interannual variations of PSCs. However, the simulated PSC areas are larger than CALIPSO observations, which can be attributed to the relatively high instrumental detection threshold of CALIPSO. SLIMCAT can capture the zonal asymmetry of PSCs in both the Antarctic and Arctic, and it can reproduce a more accurate spatial distribution of PSCs when the PSC coverage area is larger. In addition, accurate simulation of HNO_3 is important for PSC simulation. Because the simulation of denitrification processes is poor in SLIMCAT, which uses the thermodynamic equilibrium PSC scheme, the PSCs modeled by SLIMCAT are located at higher altitudes compared to the observation in the Antarctic, where the denitrification processes are strong. In contrast, for ice PSCs of which HNO_3 is not required in calculations and the Arctic where denitrification is weak, the simulated PSC at different altitudes closely matches the observations.

Keywords: polar stratospheric clouds; CALIPSO; SLIMCAT

Citation: Li, D.; Wang, Z.; Li, S.; Zhang, J.; Feng, W. Climatology of Polar Stratospheric Clouds Derived from CALIPSO and SLIMCAT. *Remote Sens.* **2024**, *16*, 3285. https://doi.org/10.3390/rs16173285

Academic Editor: Ismail Gultepe

Received: 29 April 2024
Revised: 30 August 2024
Accepted: 2 September 2024
Published: 4 September 2024

1. Introduction

Polar Stratospheric clouds (PSCs) play an important role in polar stratospheric ozone depletion [1]. Heterogeneous chemical reactions on PSC particles can transfer the chlorine, bromine, etc., from reservoir species (HCl, $ClONO_2$, etc.) to the active species (Cl, ClO, etc.), which can destroy ozone directly with sunlight. Furthermore, the denitrification and dehydration occurring on large PSC particles can prolong the lifetime of active chlorine and bromine. Airborne radar observations and laboratory studies [2–6] show that there are three main types of PSC particles: nitric acid trihydrate (NAT), supercooled ternary solution (STS), and ice PSCs. In polar winter, stratospheric sulfuric acid aerosols (SSA) start to grow by uptake of H_2O and HNO_3, and a rapid formation of STS occurs below 192 K. The NAT particles are the dominant PSC composition [7], which can efficiently form not only on pre-existing ice PSCs [8,9] but also on SSA particles containing meteoritic dust and wildfire smoke [10,11]. Homogeneous nucleation of ice PSCs takes place when the temperature is lower than the frost point, about 3–4 K [8,12]. Subsequent observations revealed that the ice PSCs can also nucleate on meteoric debris [13] and pre-existing NAT particles [14] at a higher temperature.

The above-mentioned three types of particles all play important roles in polar chemical ozone depletion. STS provides the surface for heterogeneous chemical reactions, while NAT and ice particles redistribute the HNO_3 and H_2O in the stratosphere through sedimentation

processes. The decreased HNO_3 will impede chlorine deactivation [15], while the formation of ice PSCs can irreversibly reduce the amount of H_2O in the polar vortex and lead to lower ozone depletion by reducing OH radicals [16,17]. Therefore, it is important to analyze the spatial and temporal distribution of PSCs and optimize the parameterization of PSCs in the Chemistry Transport Models (CTMs) and the Chemistry-Climate Models (CCMs) to accurately simulate stratospheric ozone chemical depletion in polar regions.

PSCs can be observed by infrared spectrometers, such as the Michelson Interferometer for Passive Atmospheric Sounding (MIPAS) [18,19] and Fourier transform spectrometer on Atmospheric Chemistry Experiment (ACE) [20,21], as well as by lidar detections [22,23]. Ground-based lidar has been observing the PSCs for almost 40 years, and it can provide observations with high temporal and vertical resolution. However, ground-based lidar is susceptible to tropospheric clouds, and it is only able to observe at specific locations, which restricts it from providing a comprehensive view of the PSCs across the polar regions [24]. In contrast, space-borne lidars, such as Cloud-Aerosol Lidar with Orthogonal Polarization (CALIOP) on Cloud Aerosol Lidar and Infrared Pathfinder Satellite Observations (CALIPSO), overcome this limitation. The depolarization rate obtained from CALIOP can effectively distinguish between spherical and non-spherical particles, which is the key factor in identifying different PSC classes [25]. Observation of PSCs from CALIPSO can help us understand the formation process of PSCs and optimize the parameterization scheme of PSCs [13,26–29].

There are two methods to simulate PSCs in numerical models. One method adopts a detailed microphysics of PSC parameterizations. For instance, Zhu et al. [26,27,30] developed a microphysical scheme for PSCs in CESM-WACCM/CARMA, including nucleation and growth processes of NAT and ice PSCs. Compared with CALIPSO observations, PSCs simulated by Zhu et al. [26,27,30] still lack a large density of small-size NAT particles induced by gravity waves. Tritscher et al. [28] included the formation and dehydration processes of ice PSCs in the Chemical Lagrangian Model of the Stratosphere (CLaMS), which makes the model can simulate the evolution of PSC particles, encompassing nucleation, growth, deposition, and evaporation. However, the model run with microphysical parameterization is computationally expensive. An alternative method is using a thermal equilibrium scheme, which assumes thermodynamic equilibrium between the particle and the gas phase [31]. The thermodynamic equilibrium schemes, which are faster than the microphysical parameterization, are used in most CTMs/CCMs and provide a good approximation of the fundamental properties of PSCs [29,32].

The SLIMCAT uses the thermodynamic equilibrium scheme to simulate heterogeneous chemistry and denitrification, which has been widely used to study chemical processes in the stratosphere [33–35] and can reproduce stratospheric chemicals as well as polar stratospheric ozone depletion well [36,37]. However, many studies using the SLIMCAT model, as well as other models, focus on the influence of PSCs on chemical species, such as O_3, H_2O, HNO_3, and HCl [32,35,38–43], while paying less attention to the characteristics of PSCs themselves. Given the importance of PSCs in ozone depletion, it is necessary to assess the SLIMCAT model's ability to simulate PSCs' features, such as area, volume, and spatial and temporal variations.

Some research evaluated the abilities of CTMs or CCMs in simulating PSCs by comparing modeled PSCs with observation only for a few days or a single year [26–29]. Few studies have paid attention to the long-term simulation of PSCs. This study focuses on the long-term simulation of PSCs in the Arctic and Antarctic from 2006 to 2021 using SLIMCAT. We conduct a thorough comparison with the observations from CALIPSO, assessing the performance of SLIMCAT in PSC simulation, and discuss the potential sources of the errors. Section 2 presents the data, model, and methods used in this paper, and Section 3 presents the results of the comparative analysis. Discussion and conclusions are presented in Sections 4 and 5, respectively.

2. Materials and Methods

2.1. CALIPSO PSC Observations

CALIOP is a dual-wavelength polarization-sensitive lidar aboard the CALIPSO polar-orbiting satellite [44], which is a joint U.S. (National Aeronautics and Space Administration, NASA) and French (Center National d'Etudes Spatiales, CNES) satellite mission launched on 28 April 2006. The lidar has three receiver channels: the 1064 nm backscatter intensity channel and the orthogonal polarization backscatter coefficients ($\beta_{\parallel}$ and $\beta_{\perp}$) at 532 nm. Pitts et al. [23,45–47] detected and classified the PSCs based on the backscatter coefficients and the scattering ratio R_{532} at 532 nm, which is defined as

$$R_{532} = \frac{\beta_{\parallel} + \beta_{\perp}}{\beta_m}, \quad (1)$$

where β_m is the molecular backscattering coefficient, calculated from the Modern-Era Retrospective analysis for Research and Applications, version 2 (MERRA-2) [48] molecular number density. There are differences between different types of PSCs in terms of shape, particle size, and physical phase state. Since non-spherical particles can cause depolarization, the $\beta_{\perp}$ can be used to distinguish between spherical and non-spherical particles. NAT and ice PSC are non-spherical solid particles, which can cause a large $\beta_{\perp}$, while STS is a spherical droplet that has a small $\beta_{\perp}$ close to 0. In addition, ice PSC particles are larger than NAT, which can produce a larger scattering ratio. Therefore, R_{532} can be utilized to distinguish NAT and ice PSC [23,46]. In the latest CALIPSO Lidar Level 2 Polar Stratospheric Cloud Mask V2.00 Product, PSCs are classified as STS, NAT-mix, Ice, NAT-enhanced, and Wave ice [23]. The vertical coverage of this PSC product ranges from 8.4 to 30 km, and the latitude coverage is 50–82°. Its vertical and along-track horizontal resolution is 180 m and 5 km, respectively. As a polar-orbiting satellite, CALIPSO passes over the polar region about 14–15 times per day, which makes CALIPSO's observations of the polar region dense enough to characterize the actual distribution of PSCs well. In addition, the CALIPSO dataset provides profiles of temperature from MERRA-2 and profiles of HNO_3 and H_2O from Microwave Limb Sounder (MLS). The dataset used in this paper is derived from the NASA Langley Research Center Atmospheric Sciences Data Center (ASDC; https://asdc.larc.nasa.gov/, accessed on 26 April 2024).

2.2. TOMCAT/SLIMCAT 3D CTM

TOMCAT/SLIMCAT (hereafter SLIMCAT) is an offline three-dimensional chemical transport model (CTM) [49] developed by the University of Leeds, United Kingdom. It contains a detailed description of stratospheric and tropospheric chemistry and is now widely used in the study of atmospheric chemical processes [34,41,50–52]. The current version of the SLIMCAT model uses a simplified PSC scheme for the simulation of heterogeneous chemistry, which assumes thermodynamic equilibrium between the particle and the gas phase [31]. Note that size distribution is important to denitrification and dehydration as the sedimentation velocity depends on particle size [53]. In the PSC scheme of SLIMCAT, the radius of NAT particles is assumed 0.5 μm, and the SAD of NAT particles is calculated based on the condensation of HNO_3. For ice PSC particles, a number density of N_{ice} = 10 cm^{-3} is assumed to calculate the SAD. Recent studies show that the model can capture well PSC processing and chlorine activation [41,43]. Here, we perform a control simulation from 2006 to 2021, including the heterogeneous chemistry processes. The temporal resolution of the SLIMCAT output data is 6 h, and daily averages are calculated. The model was forced by the European Centre for Medium-Range Weather Forecasts (ECMWF) ERA5 [54] winds and temperatures with a horizontal resolution of 2.8° × 2.8° and a total of 32 levels from the surface to ~60 km. Note that different reanalysis products, such as ERA40, ERA-Interim have been utilized to force the SLIMCAT model [49,50,55,56]. Both SLIMCAT forced by ERA-Interim and ERA5 can reproduce the spatial and temporal distribution of stratospheric ozone [56]. In comparison to ERA-Interim,

the high-resolution ERA5 shows improved ability to resolve mountain waves [28]. Therefore, the ERA5 data is better for the parameterization of PSCs in the SLIMCAT.

2.3. PSC Area Calculation

In this study, the daily SLIMCAT PSCs are present when the daily ambient temperature falls below the NAT equilibrium temperature (T_{NAT}), which is calculated by the stratospheric HNO_3 and H_2O [2]. Similarly, ice PSCs are present when the temperature is below the frost point (T_{ice}), which is calculated by H_2O [2]. The SLIMCAT PSC and ice PSC area is obtained by summing the area of the model grids where PSCs are present, hereafter referred to as the "Grid method". CALIPSO PSC data are orbital data and cannot be used to directly calculate PSC coverage area like SLIMCAT. Therefore, a statistical method introduced by Pitts et al. [23] (hereafter, the P18 method) was used to calculate the CALIPSO PSC area in this study. Firstly, the latitude range of 50−90°S or N is grouped into 10 latitude bands. Within each band, the frequency of PSC occurrence is defined as the ratio of the number of PSC observations to the total number of observations. Subsequently, this frequency is multiplied by the area of each latitude band. Finally, the areas calculated for the 10 latitude bands are summed to obtain the daily coverage area of CALIPSO PSCs. The calculation formula can be expressed as follows:

$$A_{psc} = \sum_{i=1}^{10} \frac{n_{psc,i}}{n_{obs,i}} A_i, \quad (2)$$

where i is different latitude bands, $n_{psc,i}$ is the number of PSC observations within the i-th latitude band, $n_{obs,i}$ is the total number of observations within the i-th latitude band, and A_i is the area of the i-th latitude band. As a statistical method, the sample size of observations determines the reliability of the PSC area calculated by the P18 method. There are approximately 14~15 CALIPSO orbits per day, and the satellite orbit coverage is dense in polar regions, which makes the P18 method reliable. Note that orbits are missing on some days. To avoid the area anomalies from missing orbits, only per day with orbits greater than 7 is used to calculate the PSC area in this study. In addition, CALIPSO PSC data is interpolated to 320−700 K isentropic levels at 10 K intervals before calculating the area. We will show the comparison between the P18 and the Grid method in Section 3.

2.4. Relative Standard Deviation

The relative standard deviation (RSD) is obtained by the standard deviation divided by the mean value and can be used to characterize the dispersion of a data set relative to its mean value. In this study, we used the RSD to characterize the seasonal and interannual variability in PSC volume, calculated using the following formula:

$$RSD_j = \frac{\sqrt{\frac{\sum_{i=1}^{n} (x_{ij} - \overline{x}_j)^2}{n}}}{\overline{x}_j} \times 100\%, \quad (3)$$

For the calculation of seasonal variation, j is the year, n is the total number of days (December to March for the Arctic and May to October for the Antarctic), i is the day (i = 1, 2, 3,..., n), x_{ij} is the daily PSC volume, $\overline{x}_j$ is the annual average PSC volume, and the seasonal variability is obtained by calculating the mean value of RSD_j.

For the calculation of interannual variability, j is the day, n is the total number of years, i is the year (i = 1, 2, 3,..., n), x_{ij} is the daily PSC volume, $\overline{x}_j$ is the average PSC volume on a given day over the years, and the interannual variability is obtained by calculating the mean value of RSD_j.

3. Results

Figures 1 and 2 show the seasonal evolution of the Antarctic and Arctic PSC areas observed by CALIPSO, respectively. The seasonal evolution of the Antarctic PSC area is similar from year to year. It forms near the 500 K isentropic level in middle or late May and gradually expands vertically, with cloud thickness and coverage area increasing afterward. The maximum PSC coverage area and cloud thickness typically occur during middle to late July. As the temperature increases around the 500 K isentropic level in August, the PSC coverage area gradually decreases. This decrease is accompanied by a reduction in the altitude of the maximum PSC coverage area existing, which is consistent with the downward shift in the coldest center within the polar vortex [57,58]. Although the seasonal variation of PSC coverage in the Antarctic is generally similar every year, the PSCs in each month have sizeable interannual variability, and so does the PSC duration. In most cases, PSC disappears before October, while in some years, it can persist to mid-October, which is closely related to the intensity and breakup time of the stratospheric polar vortex. In addition, the long-lasting PSC areas in 2015 and 2020 may be associated with the increasing injection of aerosols from Calbuco volcanic eruptions [59] and Australian wildfires [11]. Note that a rapid decrease in PSCs was observed in mid-September 2019, which is caused by the sudden stratospheric warming (SSW) in the Antarctic [60].

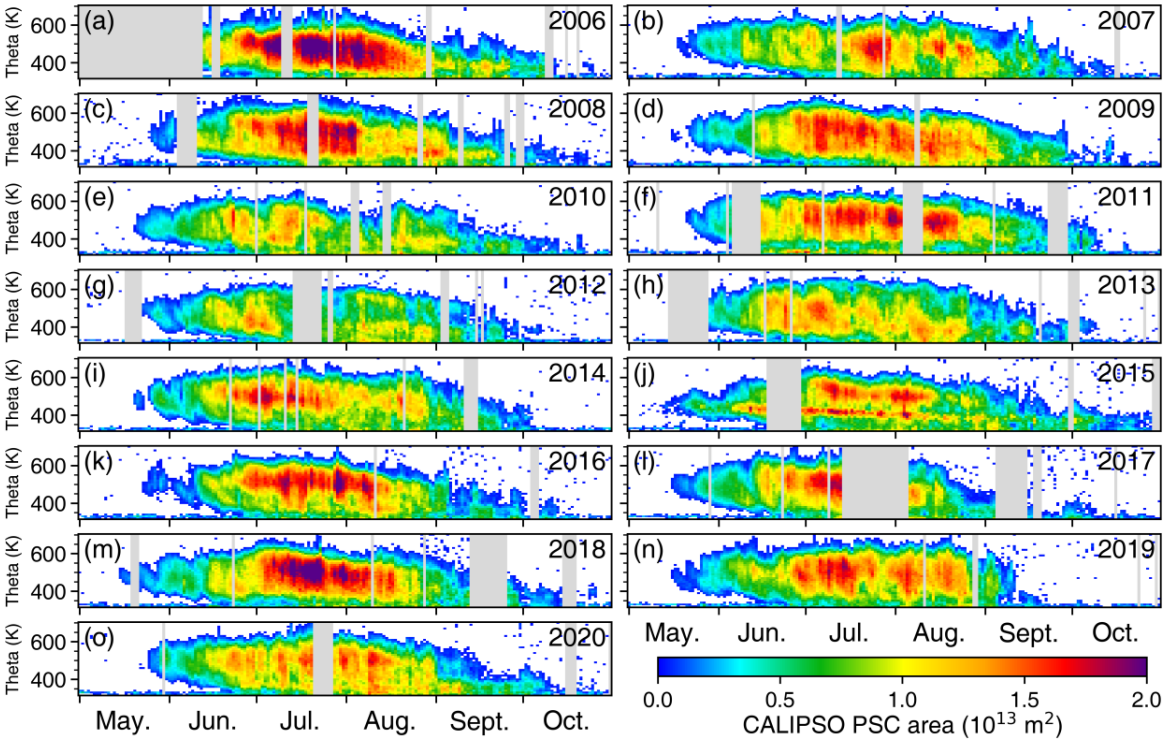

Figure 1. Seasonal evolution of the Antarctic PSC areas observed by CALIPSO during 2006−2020. The gray-filled areas indicate missing data or less than eight orbits.

The Arctic PSC coverage area (Figure 2) is much smaller than the Antarctic. This difference can be attributed to the enhanced wave propagation into the stratosphere, which is much stronger in the Northern Hemisphere due to forced waves by topography and ocean-land thermal contrast. The dissipation of planetary waves warms the polar regions and consequently leads to a smaller occurrence of PSCs. Furthermore, note that the PSC coverage area over the Arctic exhibits a much greater interannual variability in timing and duration than that over the Antarctic. This feature is closely related to the behavior of the polar vortex. For example, the PSC coverage and thickness observed during December and January 2015/2016 (Figure 2j) are the largest over the past decade due to a strong and stable Arctic stratospheric polar vortex [14], corresponding to a significant potential for

stratospheric ozone depletion. However, due to the PSC disruption caused by a major SSW occurring in late winter and major stratospheric final warming in March [61–64], no significant ozone depletion was observed in the spring of 2016. By contrast, large Arctic PSCs at 500 K persist into March in 2010/2011 (Figure 2e) and 2019/2020 (Figure 2n), which leads to severe Arctic ozone depletion in 2011 and 2020 spring [41,65]. In addition, the warmer temperature prevented the formation of PSCs in 2014/2015 and 2018/2019, so the frequency of PSC occurrence is much less in these years (Figure 2i,m).

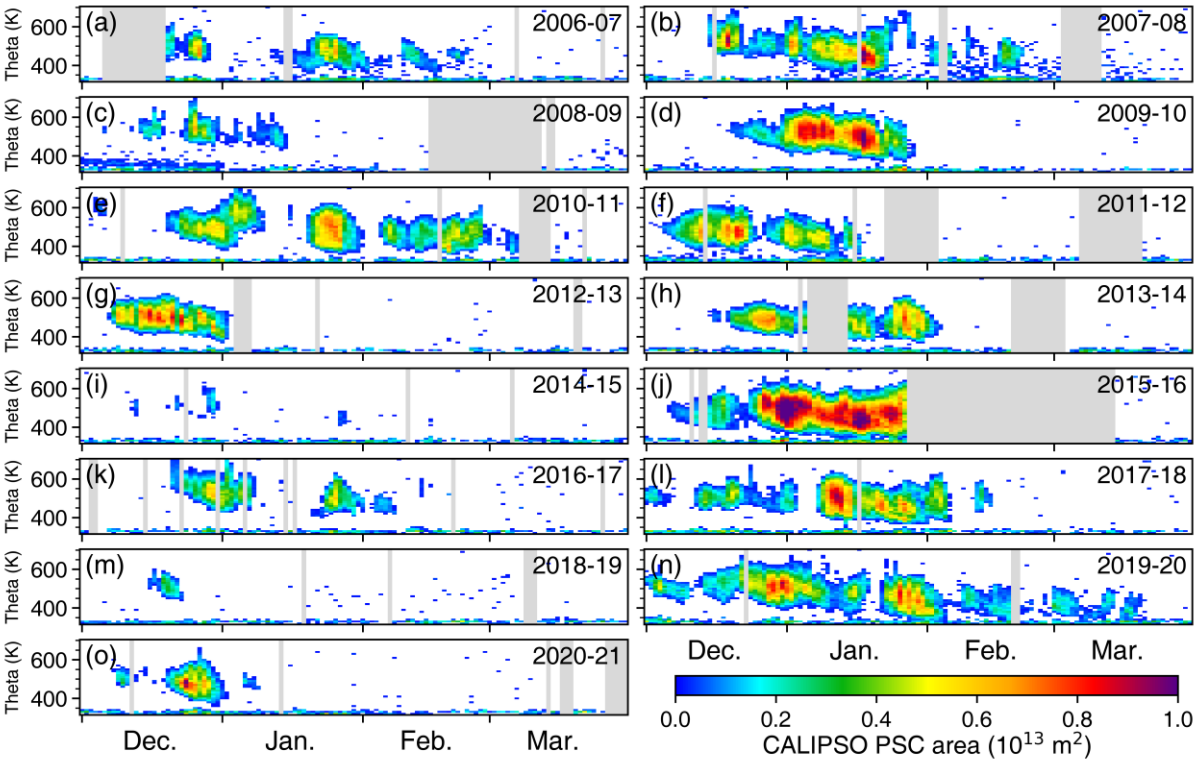

Figure 2. Same as Figure 1, but for the Arctic during 2006−2021.

Figure 3 shows the seasonal evolution of the Antarctic PSC areas simulated by the SLIMCAT model. The modeled PSC compares well with the CALIPSO observations at both seasonal and interannual time scales, e.g., the rapid decrease in mid-September 2019. However, on a daily time scale, the variability of PSC area observed by CALIPSO is relatively larger than that simulated by SLIMCAT in all years. In addition, we found that the modeled PSC maximum areas are ~5 million km^2 (~25%) larger than CALIPSO observation, and it forms earlier and persists for a longer period compared with CALIPSO observation. The discrepancies between the observation and model simulation will be discussed in the following text. In the Arctic, the SLIMCAT effectively captures the large seasonal and interannual variability of PSCs (Figure 4). Note that the modeled PSCs reproduce the extensive PSC formation observed in early winter during 2015/2016 and the long-lasting existence of PSCs in 2010/2011. However, SLIMCAT also overestimates the PSC area and its duration in the Arctic. Figure S1 shows the seasonal variation of the Antarctic and Arctic PSC area climatology from CALIPSO observations (a, b) and SLIMCAT simulations (c, d). Although the simulated PSC areas are larger than the CALIPSO observations, the SLIMCAT simulations effectively capture the seasonal variations of PSCs in both the Antarctic and Arctic.

There are two possible explanations for the larger PSC coverage in SLIMCAT than CALIPSO. The main reason is the higher instrument detection threshold of CALIPSO. In the SLIMCAT, the PSC parameterization is based on thermodynamic equilibrium theory, which assumes the existence of PSCs when the environmental temperature is lower than T_{NAT}. Considering the number density of PSC particles increases as the temperature decreases,

SLIMCAT simulates the occurrence of PSCs in certain regions when the temperature is slightly below T_{NAT}. However, the lower number density and backscatter of the thinner PSCs may prevent the PSCs from being detected by CALIPSO [30,45], which results in a larger PSC coverage area in SLIMCAT than in CALIPSO. To verify this, we recalculated PSCs along the orbital profile (Figures S2 and S3) based on the thermodynamic equilibrium method using MERRA2 temperature, H_2O, and HNO_3 provided by MLS data. Similar to the simulation of PSCs by SLIMCAT, the range of PSCs obtained through the thermodynamic equilibrium method using observed temperature, H_2O, and HNO_3 data is larger than direct CALIPSO observations. MIPAS is more sensitive and able to detect the presence of PSCs earlier compared to CALPSO [7]. Figure S4 shows the climatology of the PSC area derived by MIPAS during 2002−2012. Although the seasonal variability of the MIPAS PSC is significantly different from that of the CALIPSO and SLIMCAT PSCs, its maximum coverage area is larger than that of CALIPSO and closer to that of SLIMCAT. Tritscher et al. [7] also showed that the volume of the MIPAS PSC is larger than that of the CALPSO PSC by a factor of 1.38 in the Antarctic and 1.63 in the Arctic. The comparison with MIPAS indicates that CALIPSO, which has a high instrumental detection threshold, may underestimate PSCs. Besides, in the CALIPSO PSC detection algorithm, the PSCs are detected by statistical anomalies of stratospheric background aerosols [47]. However, some PSCs may be misclassified as background aerosols or as "sub-visible" PSCs [10,23], resulting in an underestimation in CALIPSO. Even so, we still use the direct observation by CALIPSO as the standard for PSCs in the following analysis since there is no alternative long-term PSC observation. Another reason could be the relatively low resolution of SLIMCAT ($2.8° \times 2.8°$). Once $T < T_{NAT}$, the PSCs are considered to fill the entire grid, and the nucleation and growth times of the particles are ignored, which can lead to an overestimation of the simulated PSC area.

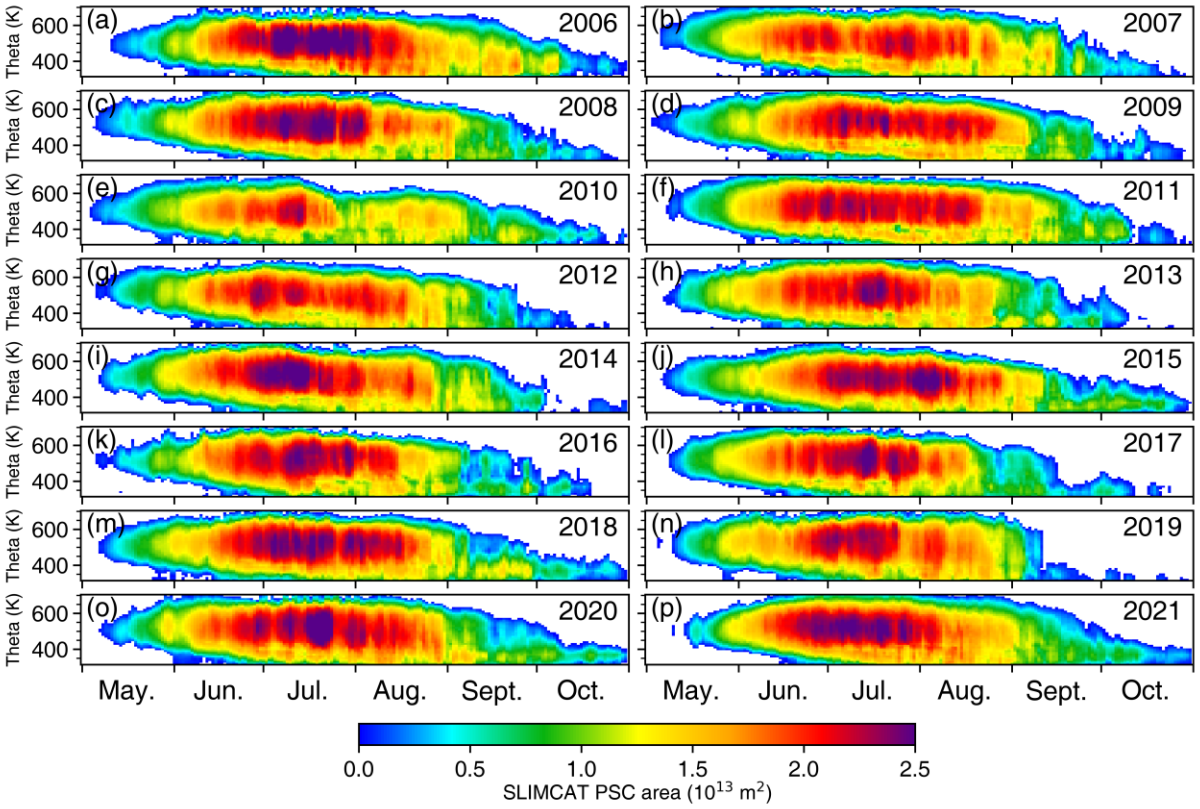

Figure 3. Seasonal evolution of the Antarctic PSC areas calculated by SLIMCAT model simulation during 2006−2021.

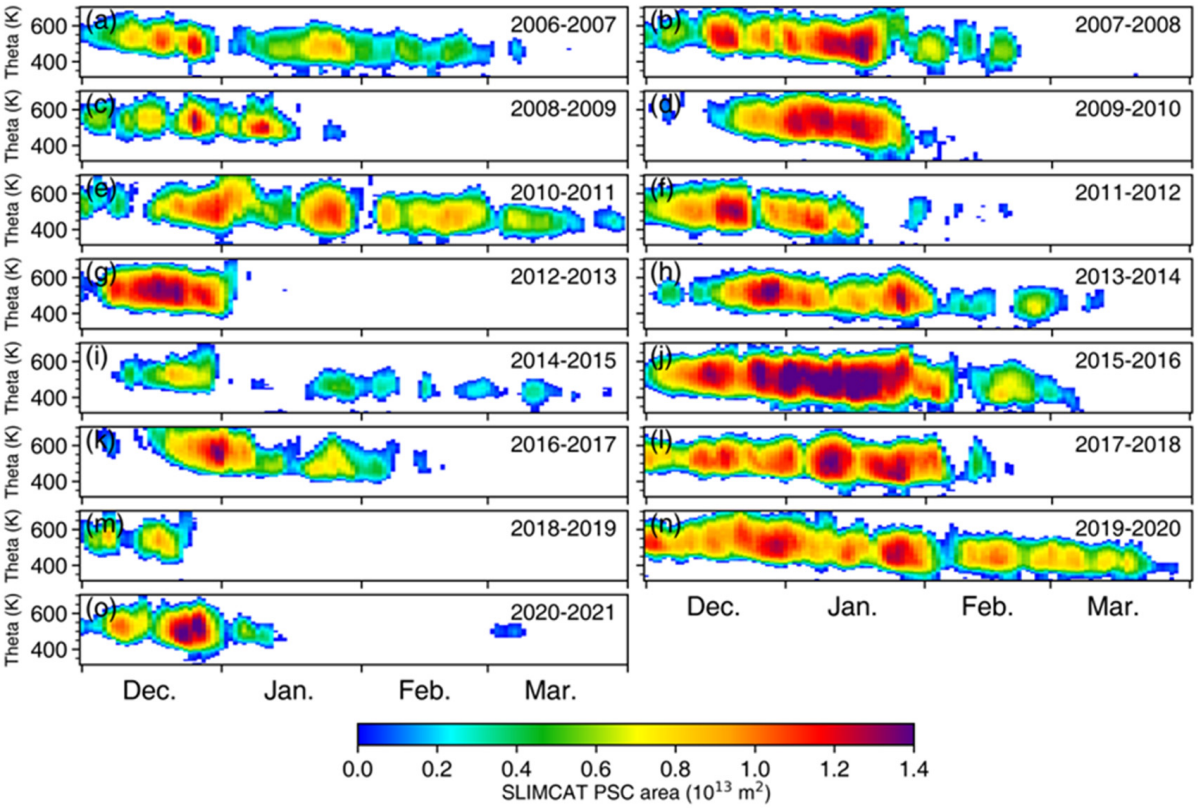

Figure 4. Same as Figure 3, but for the Arctic during 2006−2021.

In addition, the method of calculating the PSC area may also cause errors. Steiner et al. [29] interpolated the CALIPSO observation data into the model grid and found that the PSC coverage area calculated by the Grid method is larger than that calculated by the P18 method. The CALIPSO daily orbits do not cover all the model grids in the polar regions, and the CALIPSO missing grids may be PSC-existing. To address this issue, Steiner et al. [29] utilized grids with orbit coverage at the same latitude to fill in the missing grids. This method is suitable for the Antarctic region as the spatial distribution of PSCs exhibits a weaker zonal asymmetry. However, in the Arctic region, there is a notable zonal asymmetry in the spatial distribution of PSCs, which makes the P18 method unsuitable. In this study, we interpolate the SLIMCAT PSCs to the CALIPSO orbits and recalculated the SLIMCAT PSC coverage using the P18 method (Figures S5 and S6). Note that the values of the modeled PSC area using P18 method are almost the same as those using the Grid method. To compare the difference between the two calculation methods more clearly, Figure S7 shows a contrast between the SLIMCAT PSC areas calculated by the P18 method and the Grid method. Overall. The points at both the North and South Poles are distributed near the diagonal, indicating that the difference in PSC area calculated by the two methods is small. In this case, the use of the P18 method resulted in a decrease in the Antarctic PSC area of 0.71 million km^2 (relative error: −6.10%) and an increase in the Arctic area of 0.15 million km^2 (relative error: 3.14%) compared to the Grid method, indicating that the PSC area calculated by the P18 method is reasonable. This result is not consistent with that of Steiner et al. [29], which may be related to the interpolation process. Steiner et al. [29] interpolated PSCs from high-resolution orbital points to low-resolution grids, where a single PSC may occupy an entire grid, resulting in an increase in PSC coverage area. In contrast, in this study, interpolation from low-resolution grid points to high-resolution orbital points avoids this issue. However, after applying the P18 method, the daily variation in the SLIMCAT PSC area increases, which may be related to the daily variation in CALIPSO orbits. To avoid this problem, all SLIMCAT PSC areas still use the Grid method in this paper, while the CALIPSO PSC areas are calculated using the P18 method.

The polar-averaged volume of PSCs is obtained by vertically integrating the PSC area in the altitude coordinate. It is an indicator of the total area coverage of PSCs at all heights in the lower stratosphere. Figure 5 shows the seasonal evolution of PSC volume in the Antarctic and Arctic. The climatological PSC volume in the Antarctic reaches its maximum value around mid-July in both CALIPSO observation and SLIMCAT simulation, consistent with the maximum time in PSC area and thickness (Figures 1 and 3). However, the modeled climatological maximum PSC volume is approximately 60% larger than that observed by CALIPSO, primarily due to the larger PSC area in SLIMCAT. Furthermore, in the Antarctic late winter and spring, SLIMCAT can reproduce the years when the daily minimum and maximum PSC volume occur (Figure 5a,b). In the Arctic, years with the maximum PSC volume are nearly consistent between CALIPSO and SLIMCAT. The climatological maximum PSC volume is approximately 20 million km^3, which is significantly smaller than the 150 million km^3 in Antarctica. The climatological Arctic PSC volume and interannual standard deviation reach their maximum values during January in both model and observation. Particularly note that the maximum daily volume of the Arctic PSCs in January often occurred in 2015 and 2016. The PSCs in these two years are significantly larger than the multi-year average volume. Besides, the model simulation and CALIPSO are in close agreement for seasonal variation of PSC volume. However, the modeled climatological maximum PSC volume is about 200% larger than that observed by CALIPSO, and it shows larger fluctuations in February and March.

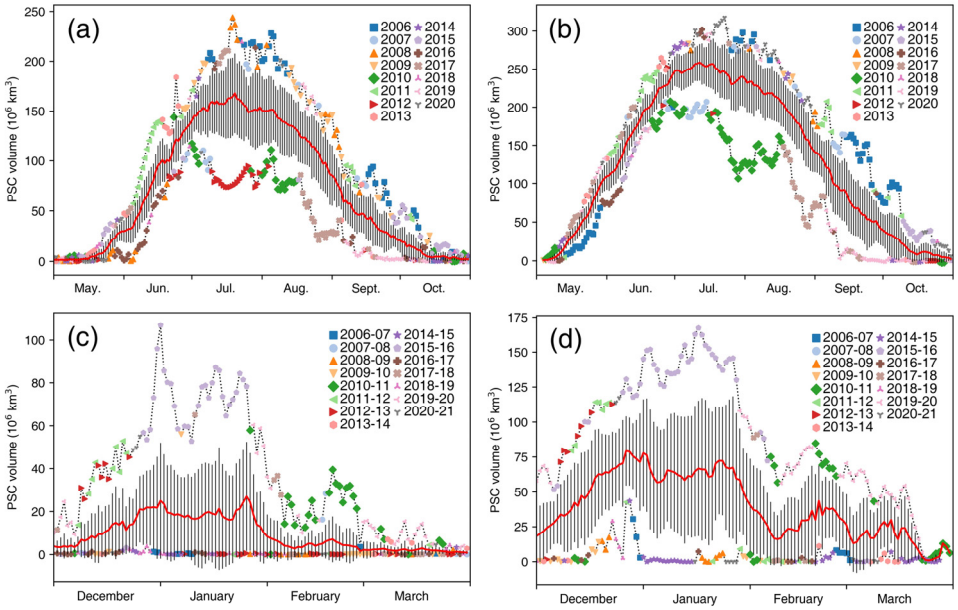

Figure 5. Time series of PSC volume in the Antarctic during 2006−2020 (**a**,**b**) and the Arctic during 2006−2021 (**c**,**d**) derived from CALIPSO observation (**a**,**c**) and SLIMCAT simulation (**b**,**d**). The thick red line indicates the climatological mean PSC volume, the black vertical lines indicate the standard deviation of the 14-year PSC volume, and the dashed lines and colored markers indicate the record maximum and minimum values for the period.

Table 1 summarizes the mean value, seasonal variability, interannual variability, and long-term trends in PSC volumes from CALIPSO observations and SLIMCAT simulations. The volume of both Antarctic and Arctic PSCs simulated by SLIMCAT is larger than that observed by CALIPSO. Note that the seasonal variability and the interannual variability of the modeled PSC volume are smaller than that of the observed, indicating a smaller variability in SLIMCAT PSCs than that in CALIPSO PSC. In addition, both observations and simulations show that the seasonal variability and interannual variability of PSC volume in the Arctic is much larger than that in the Antarctic, which is consistent with that of the PSC area. The long-term trend is calculated from the annual average volume (average

of December to March in the Arctic and May to October in the Antarctic), and there is a large difference between the long-term trends of the observed and modeled Antarctic PSC volumes in the table. The CALIPSO observed Antarctic PSC volume shows a slight decline, whereas the SLIMCAT simulated PSC volume has a trend close to zero. It should be noted that none of the linear trends in the table are statistically significant, indicating no significant trend in the annual average PSC volume.

Table 1. Summary of PSC volumes for the Antarctic during 2006−2020 and the Arctic during 2006−2021 from CALIPSO observations and SLIMCAT simulations.

Items	Antarctic		Arctic	
	CALIPSO	**SLIMCAT**	**CALIPSO**	**SLIMCAT**
Mean value (10^6 km^3)	71.72	135.49	9.82	46.84
Seasonal variation (%)	86.39	67.49	148.23	75.08
Interannual variation (%)	41.12	36.02	128.92	74.95
Linear trend (10^6 km^3/year)	-1.21 ± 1.40	0.07 ± 0.89	0.05 ± 0.58	0.39 ± 1.96

Figure 6 shows the Antarctic PSCs observed by CALIPSO and the spatial distribution of T−T_{NAT} on 470 K isentropic level derived from the SLIMCAT. We note that the SLIMCAT model reproduces the key features of the PSCs distribution. In particular, the modeled PSCs are in good agreement with the observation when the PSC areas are large, such as in 2008 and 2011. However, in the years with fewer PSCs, such as 2017, the modeled PSCs are significantly larger than the CALIPSO observation. In the Arctic (Figure 7), T_{NAT} isolines (green lines) also cover a larger area than CALIPSO observation (yellow dots) in most cases. If we take the T_{NAT}−3 K as the threshold of PSC formation, the region enclosed by the orange contour line is in better agreement with the observed PSC distribution. It should be noted that we do not consider the use of T_{NAT}−3 K as the threshold for PSC formation in the model to be a better choice. In some cases, although the boundaries of PSCs coincide closely with the orange contour line, there are still a significant number of PSC occurrences between the green and orange contours. Due to the good agreement between the modeled PSCs with T_{NAT}−3 K as a threshold and the observations, we will later utilize this to compare with the observations.

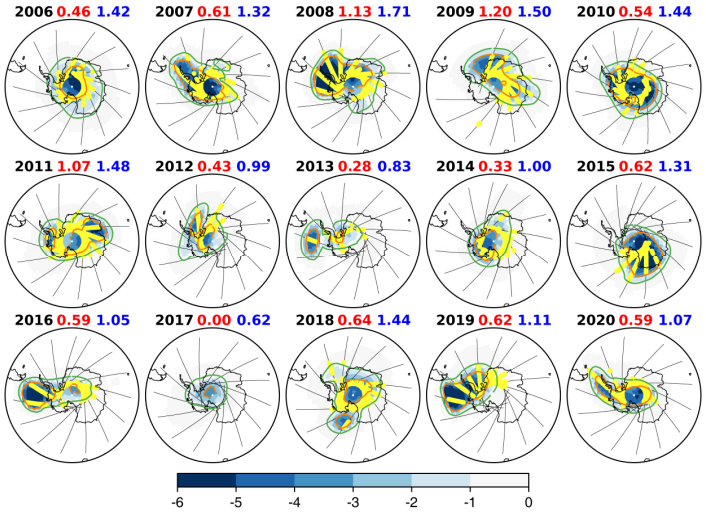

Figure 6. The spatial distribution of T−T_{NAT} calculated by SLIMCAT simulation (shadings) and PSCs observed by CALIPSO directly (yellow dots) on September 1 from 2006 to 2020. The black lines indicate the orbit of CALIPSO during a day on 470 K isentropic level. The green and orange lines indicate T = T_{NAT} and T −T_{NAT} = −3 K, respectively. PSC areas calculated by SLIMCAT and CALIPSO are shown at the top of each panel, where the red numbers indicate the CALIPSO area and the blue numbers indicate the SLIMCAT area in units of 10^7 km^2.

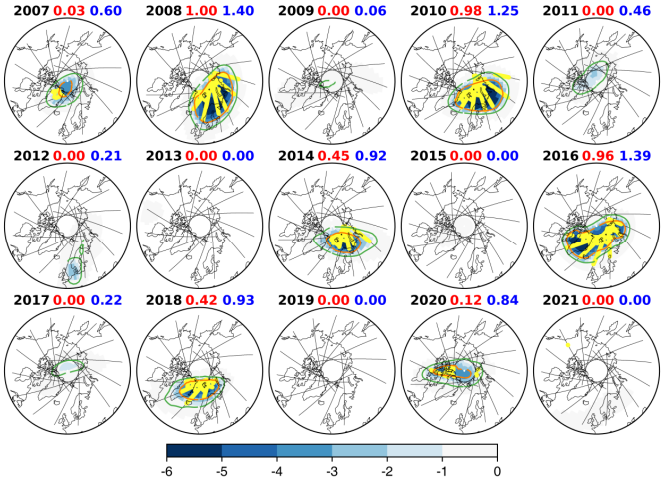

Figure 7. Same as Figure 6, but for the Arctic on January 18 from 2006 to 2021.

Figure 8 shows the PSC area on different isentropic levels derived from CALIPSO and SLIMCAT. To eliminate the impact of zero values on the regression line, the data with zero PSC area for both CALIPSO and SLIMCAT are removed. The modeled PSC coverage areas over the Antarctic and Arctic regions are both larger than the CALIPSO observation, and thus, the SLIMCAT values are located at the left upper corner of the diagonal. Note that the slope of the linear fit line is 1.14 and 1.45 in the Antarctic and Arctic, respectively, suggesting that the simulated PSCs in the Antarctic have a better correlation with observed values. According to the regression coefficient, the modeled PSC coverage area is about 5.43 million km^2 (relative error: 113%) larger than the CALIPSO observation in the Antarctic, while it is about 3.44 million km^2 (relative error: 269%) larger in the Arctic.

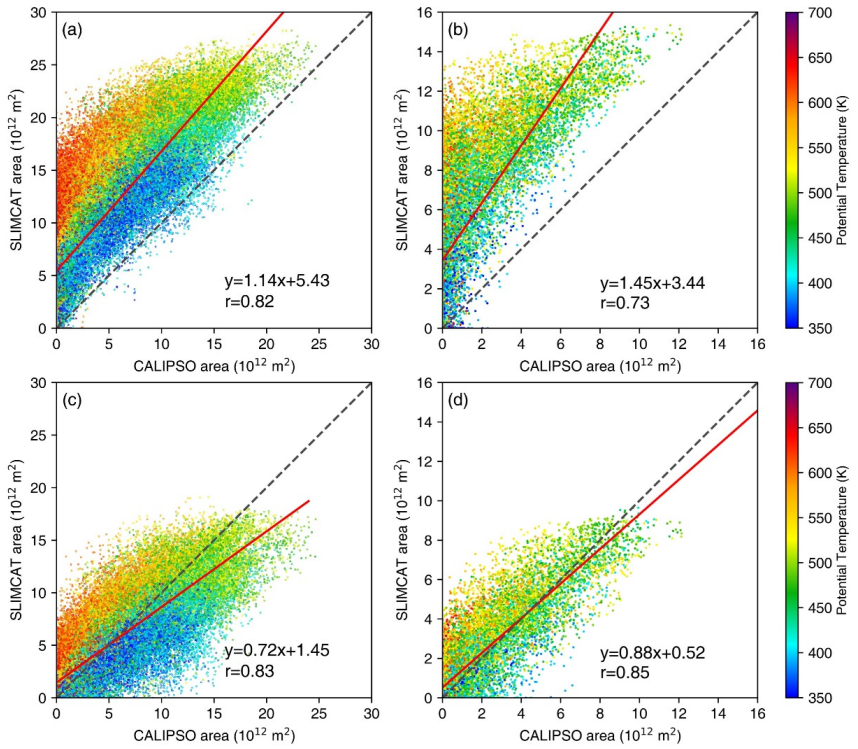

Figure 8. Modeled daily PSC area plotted against CALIPSO observation in the Antarctic (**a**,**c**) and Arctic (**b**,**d**). The thresholds for PSC formation in SLIMCAT are T_{NAT} (**a**,**b**) and $T_{NAT}-3$ K (**c**,**d**), respectively. Different colors indicate PSCs on different isentropic levels. The dashed line is the diagonal. The linear fits are shown as red solid lines. The linear fit equations and correlation coefficients are shown at the bottom right on each panel.

In the Antarctic, the modeled PSC coverage area in the middle stratosphere is much larger than the observation, while it is gradually closer to the observation as altitude decreases. Figure 8c shows that the adjusted modeled PSC area using $T_{NAT}-3$ K is larger on the high isentropic levels and smaller on the low isentropic levels, suggesting that the occurrence altitude of the modeled PSCs is higher than that in observation. This discrepancy between the simulation and observation may be caused by poor simulation of PSC sedimentation processes of the simplified PSC scheme in SLIMCAT. Feng et al. [66] found that the simplified PSC scheme in SLIMCAT could potentially result in an overestimation of denitrification, which may be the main reason for this disparity between the model and observation. In the Arctic, points at different levels are more uniformly concentrated around the linear fit lines compared to the Antarctic, indicating that the discrepancy between model and observation is less dependent on levels (Figure 8d).

Figure 9 shows the PSC occurrence frequency on 500 K isentropic level at which the maximum PSC is located. The CALIPSO observation indicates that the PSC occurrence frequency in the Antarctic reaches its peak value in July and subsequently decreases gradually. Due to the steady descent of air masses over the Antarctic stratosphere during spring [57,58], there are no PSCs at 500 K in October, and most of the PSCs are located below the 400 K isentropic level (Figure 1). Furthermore, the maximum PSC frequency occurs near the Antarctic Peninsula. The high-frequency mountain wave activity near the Antarctic Peninsula results in local temperature fluctuations, which rapidly decreases the ambient temperature below T_{ice} and leads to ice nucleation. These ice particles further induce NAT nucleation [19,23,67]. Compared to the CALIPSO observation, the SLIMCAT simulation shows a higher PSC occurrence frequency, and the relative bias can reach 100% over the entire Antarctic region. Additionally, the SLIMCAT simulations can reproduce the zonal asymmetry in PSC occurrence frequency, with higher PSC occurrence frequency in May and September near the Antarctic Peninsula, which is not significant in July. However, the PSC frequency with $T_{NAT}-3$ K as the threshold of PSC formation (Figure 9c) is significantly smaller, and there is a significant zonal asymmetry in July. Therefore, the possible reason for the insignificant asymmetry of SLIMCAT PSC frequency in July is that the PSC frequency reached nearly 100% over the Antarctic continent, which overshadows and masks this underlying asymmetry.

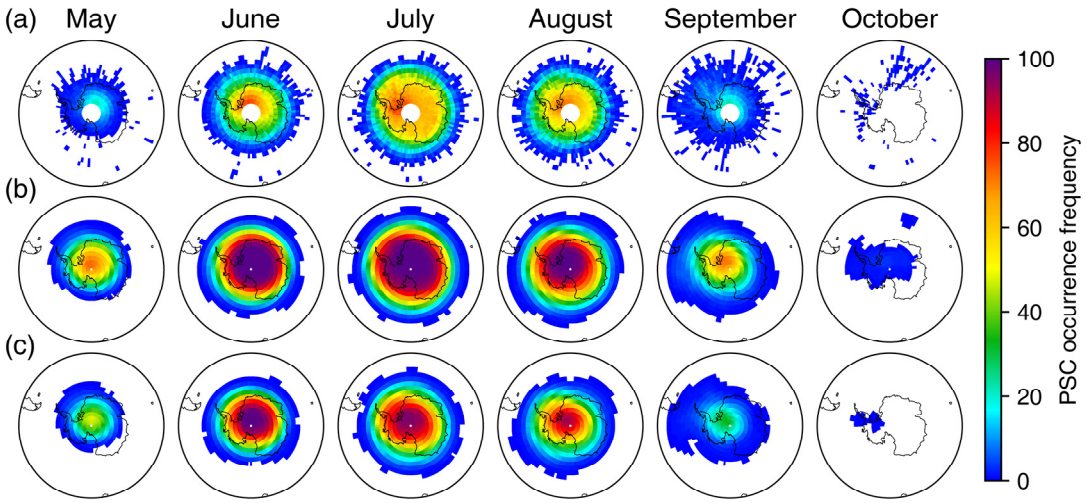

Figure 9. The PSC occurrence frequency from May to October for the period 2006–2020 at 500 K isentropic levels in the Antarctic derived from (**a**) CALIPSO observation, (**b**) SLIMCAT simulation, and (**c**) SLIMCAT simulation with $T_{NAT}-3$ K as the threshold of PSC formation.

Figure 10 shows the PSC occurrence frequency in the Arctic region on 460 K isentropic level from December to March based on CALIPSO observation and SLIMCAT simulation. Due to the higher temperature in the Arctic, the PSC occurrence frequency is notably

lower than that in the Antarctic. The PSC occurrence frequency shows a noticeable zonally asymmetric structure, with the maximum frequency between the Svalbard Archipelago and Novaya Zemlya, which is related to the location of the climatological polar vortex center [68]. The CALIPSO observed PSC occurrence frequency reaches its maximum in January, while the modeled maximum PSC occurrence frequency is also in January but significantly higher than the CALIPSO observation.

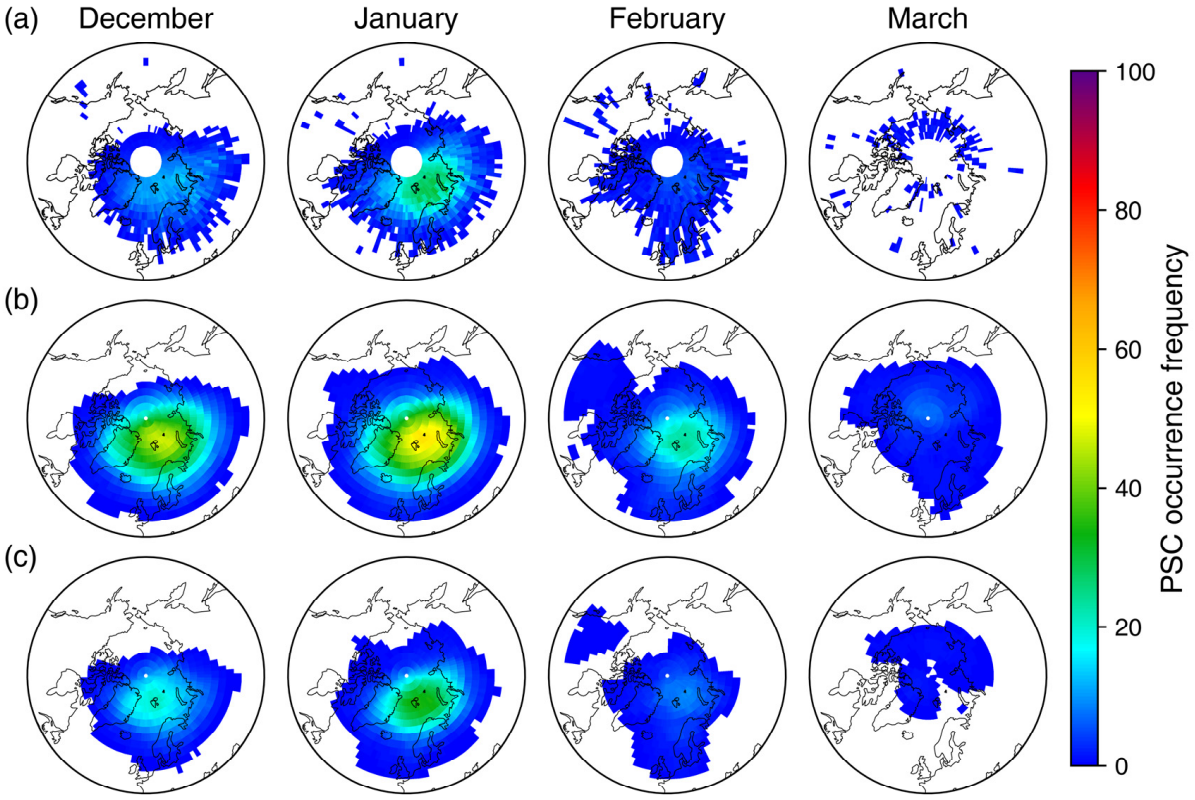

Figure 10. Same as Figure 9, but from December to March for the period 2006−2021 at 460 K isentropic levels in the Arctic derived from (**a**) CALIPSO observation, (**b**) SLIMCAT simulation, and (**c**) SLIMCAT simulation with $T_{NAT}-3$ K as the threshold of PSC formation.

Figure 11 shows the seasonal evolution of Antarctic ice PSC areas observed by CALIPSO. Since ice PSCs rarely occur in the Arctic, only the Antarctic PSCs are shown. Influenced by the temperature inside the polar vortex, the interannual variability of ice PSC area over the Antarctic is large, and its seasonal evolution differs from that of total PSCs (Figure 1). The seasonal variation of ice PSCs in the Antarctic is characterized by periodic extreme values occurring every few days. This phenomenon can be attributed to the requirement of very low temperatures for ice PSC formation. The synoptic-scale variations in the polar vortex significantly influence the occurrence of ice PSCs. Ice PSCs usually appear in June and disappear before October. Figure 12 shows the seasonal evolution of Antarctic ice PSC areas derived from SLIMCAT simulation. Although the modeled ice PSC areas are larger than those observed by CALIPSO, the modeled ice PSCs can capture its interannual variability, as well as several large ice PSC events (e.g., 2013, 2016, 2018, and 2020).

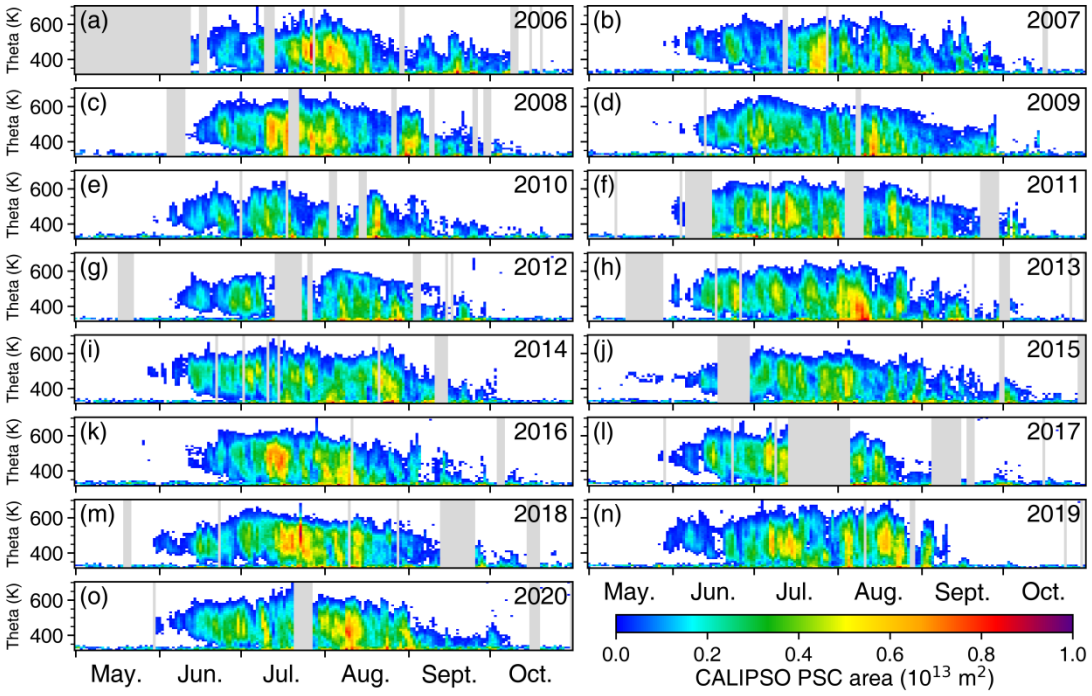

Figure 11. Seasonal evolution of the Antarctic ice PSC areas observed by CALIPSO during 2006−2020. The gray-filled areas indicate missing data or less than eight orbits.

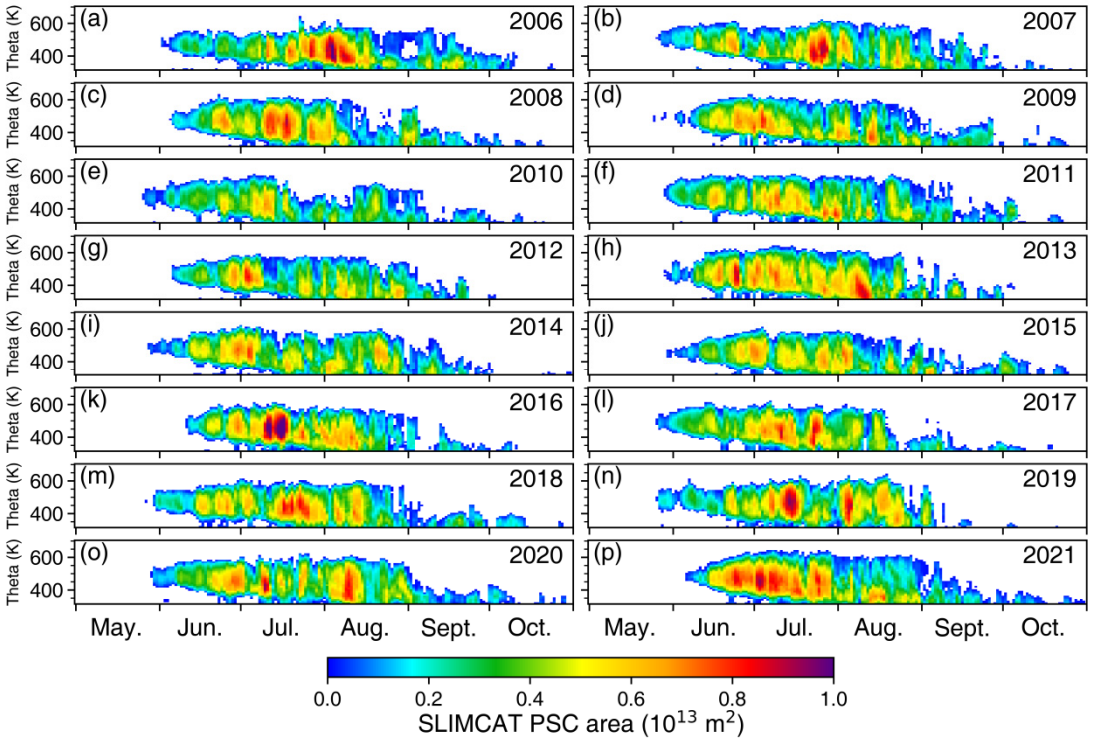

Figure 12. Same as Figure 11, but derived from SLIMCAT simulation during 2006−2021.

Figure 13 shows the ice PSC area on different isentropic levels derived from CALIPSO and SLIMCAT. Although the modeled ice PSCs are larger than the observation, the correlation coefficient between SLIMCAT and CALIPSO is 0.86, and the absolute error (0.35 million km^2) and relative error (35%) are smaller than that of total PSCs (Figure 8), indicating that the modeled ice PSC areas are in better agreement with the observation. The large ice PSC areas are located

around 450 K, which is lower than the level at the maximum coverage of total PSC locates. In addition, the points of ice PSC area at different levels are uniformly concentrated around the linear fit lines, indicating that the altitude of the modeled ice PSCs agrees well with the observed one. Since T_{ice} depends only on H_2O, while T_{NAT} depends not only on H_2O but also on HNO_3, the altitude discrepancy in Figure 8a,c between simulations and observations can be attributed to the HNO_3 simulation bias and insufficient simulation of the NAT sedimentation. It also indicates that the role of HNO_3 (as well as H_2O) in PSC calculations cannot be ignored. Thus, it is not accurate to employ fixed HNO_3 and H_2O for PSC threshold temperatures or even use 195 K as the threshold temperature for PSC formation, which may have considerable discrepancies. We experimented with using 195 K as the threshold temperature for PSC formation (Figure S8), and the discrepancy between simulations and observations is much larger than that in Figure 8a,b, which suggest that the simulation of PSCs can be effectively improved after considering realistic HNO_3 and H_2O.

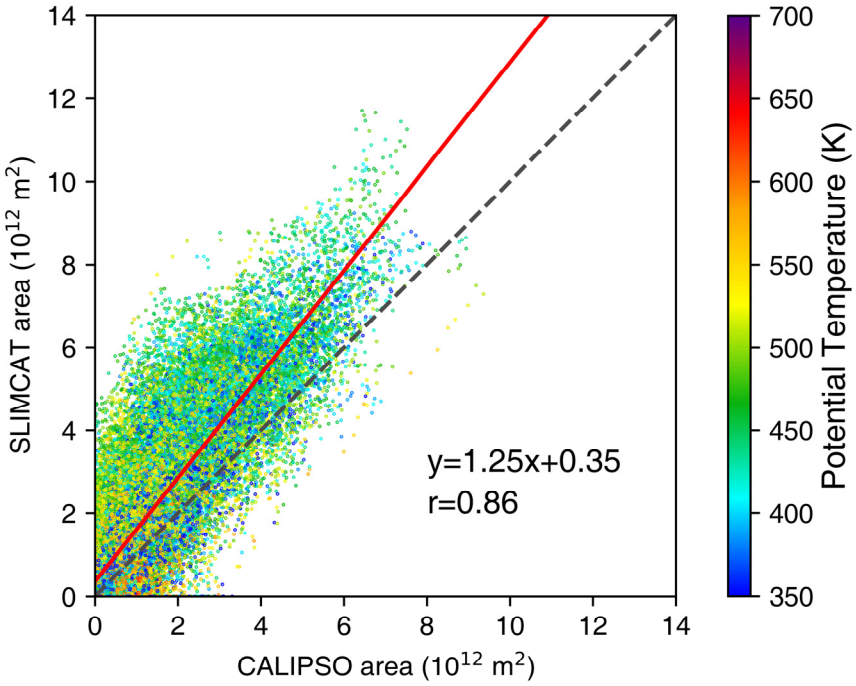

Figure 13. Modeled daily ice PSC area plotted against CALIPSO observation in the Antarctic. Different colors indicate ice PSCs on different isentropic levels. The dashed line is the diagonal. The linear fit is shown as the red solid line. The linear fit equation and correlation coefficient are shown in the bottom right of the panel.

4. Discussion

There is a better agreement between the simulated and observed spatial distribution of PSCs when the $T_{NAT}-3$ K is used as the threshold temperature for PSC formation. A sensitivity experiment conducted by Steiner et al. [29] involved offsetting a cold temperature bias in the polar lower stratosphere by +3 K, resulting in a significantly improved agreement between the simulated PSC coverage area and observed from CALIPSO. Furthermore, Pitts et al. [45] found that the agreement between the observed CALIPSO PSC area and the area of $T < T_{STS}$ (assuming T_{STS} is 4 K colder than T_{NAT}) is better than that with the area of $T < T_{NAT}$. Observation indicates that when the temperature is slightly below T_{NAT}, the number of NAT is relatively small, which cannot be detected. As the temperature decreases, the number of NAT peaks at approximately 3–4 K below T_{NAT}, primarily due to different exposure times of air parcels below T_{NAT} [23,32,46,69]. In contrast, for STS and ice PSCs, the peak occurs rapidly once the temperature is below the respective formation threshold temperatures, T_{STS} and T_{ice}. In thermodynamic equilibrium models, PSCs take place once the temperature falls below the threshold temperature. As a result, using T_{NAT} as the threshold of PSC formation leads to a

larger simulated PSC area than the observation, while using T_{ice} for ice yields better agreement with observations of ice PSCs. Although the use of T_{NAT}–3 K as a threshold for PSC formation has significantly improved the simulation, it is not a good decision to adjust the PSC formation threshold in the model to cater to the CALIPSO observations.

In addition, our results indicate that accurate simulation of HNO_3 (as well as H_2O) is crucial for PSC simulation. The simplified PSC scheme in SLIMCAT still exhibits deficiencies in simulating HNO_3 [66]. Considering the critical role of HNO_3 in the PSCs and the conversion of active chlorine to chlorine reservoir species in spring [15], it is necessary to improve the simulation of denitrification. In future model development, denitrification schemes with detailed microphysical schemes where the air parcel is moving along the trajectory in Lagrangian can be included to improve the simulation of PSCs as well as ozone.

5. Conclusions

Using a CTM (SLIMCAT), we simulate the PSCs in the North and South Polar stratosphere and compare the features of PSCs, including their area, volume, and distribution, to the observed PSCs from the CALIPSO satellite. We use two different methods to calculate the SLIMCAT (Grid method) and CALIPSO (P18 method) PSC areas. Although Steiner et al. [29] suggested that the two methods lead to relatively large differences in PSC area, our results show that the modeled PSC areas calculated by the two methods are close.

The seasonal evolution of the Antarctic PSC area is similar from year to year. It forms near the 500 K isentropic level in middle and late May, and then its area gradually increases. After reaching a maximum in middle and late July, the PSC area begins gradually to decrease until it disappears in October. In contrast, the year-to-year variability in PSC coverage area, timing, and duration in the Arctic is much larger. There is a zonal asymmetry in the spatial distribution of PSCs, especially in the Arctic. The maximum occurrence frequency of the Antarctic PSCs is near the Antarctic Peninsula, which is influenced by topographic gravity waves. In the Arctic, the maximum occurrence frequency is between the Svalbard and Novaya Zemlya, which is related to the location of the climatological polar vortex center.

The SLIMCAT agrees well with the observation of seasonal variation and spatial distribution of PSCs. However, the SLIMCAT simulations overestimate the PSC coverage, with the simulated PSCs appearing earlier and persisting for a longer duration. There are several factors contributing to the discrepancy between simulated and observed PSCs. One is the high detection threshold of CALIPSO, which leads to the thin PSC layer not being monitored. Additionally, the discrepancy may also stem from the coarse resolution of SLIMCAT. Comparing the spatial distribution of PSCs from SLIMCAT simulation with CALIPSO observation, we found that the simulated spatial distribution of PSCs is consistent with the observation when the PSC coverage area is larger. However, when the PSC coverage area is smaller, the observed PSC coverage area is significantly larger than the simulated results. Finally, our results indicate that accurate simulation of HNO_3 (as well as H_2O) is crucial for PSC simulation.

Supplementary Materials: The following supporting information can be downloaded at: https://www.mdpi.com/article/10.3390/rs16173285/s1, Figure S1. Seasonal variations in the climatology of the PSC area derived by (a,b) CALIPSO during 2006−2020, (c,d) SLIMCAT during 2006−2020 in the Antarctic (left) and Arctic (right). The range of the color bar is 0 to 1.4 for the Arctic and 0 to 2.1 for the Antarctic; Figure S2. The difference in T and T_{NAT} (color shading) along the 10th orbital profile on June 14, 2006. Regions where $T-T_{NAT} < 0$ indicate the presence of PSCs. PSCs directly observed by CALIPSO are shown in black-dotted regions; Figure S3. Same as Figure S2, but for PSCs on 15 June 2006; Figure S4. Seasonal variation in the climatology of the PSC area derived by MIPAS during 2002−2012 in the Antarctic (a) and Arctic (b). The range of the color bar is 0 to 1.4 for the Arctic and 0 to 2.1 for the Antarctic; Figure S5. Seasonal evolution of the Antarctic SLIMCAT PSC areas calculated by P18 method during 2006−2020. The gray-filled areas indicate missing data or less than eight orbits; Figure S6. Same as Figure S5, but for the Arctic; Figure S7. The SLIMCAT PSC

area was calculated using the Grid method and plotted against the SLIMCAT PSC area, which was calculated using the P18 method in the Antarctic (a) and the Arctic (b). Different colors indicate PSCs on different isentropic levels. The linear fits are shown as solid red lines. The linear fit equations and correlation coefficients are shown at the bottom right of each panel. The gray area indicates that 95% of the points fall into this region; Figure S8. The PSC area using 195 K as the formation threshold is plotted against CALIPSO observation in the Antarctic (a) and Arctic (b). Different colors indicate PSCs on different isentropic levels. The linear fits are shown as solid red lines. The linear fit equations and correlation coefficients are shown at the bottom right of each panel.

Author Contributions: Conceptualization, J.Z.; methodology, D.L. and J.Z.; Software, D.L. and W.F.; Investigation, D.L. and Z.W.; Writing—original draft preparation, D.L., Z.W., S.L., J.Z. and W.F.; Writing—review & editing, D.L., Z.W., S.L., J.Z. and W.F.; Project administration, J.Z.; Funding acquisition, J.Z. All authors have read and agreed to the published version of the manuscript.

Funding: This research was funded by National Natural Science Foundation of China (Jiankai Zhang, 42075062 and 42130601), and the Fundamental Research Funds for the Central Universities (Jiankai Zhang, lzujbky-2021-ey04).

Data Availability Statement: The CALIPSO dataset is available at https://asdc.larc.nasa.gov/data/CALIPSO (accessed on 26 April 2024).

Acknowledgments: We thank Martyn P. Chipperfield for model support. We gratefully acknowledge the scientific teams for CALIPSO PSC data. We also thank the ECMWF for providing ERA5 data. We appreciate the computing support provided by Supercomputing Center of Lanzhou University.

Conflicts of Interest: The authors declare no conflicts of interest.

References

1. Solomon, S.; Garcia, R.R.; Rowland, F.S.; Wuebbles, D.J. On the Depletion of Antarctic Ozone. *Nature* **1986**, *321*, 755–758. [CrossRef]
2. Hanson, D.; Mauersberger, K. Laboratory Studies of the Nitric Acid Trihydrate: Implications for the South Polar Stratosphere. *Geophys. Res. Lett.* **1988**, *15*, 855–858. [CrossRef]
3. Browell, E.V.; Butler, C.F.; Ismail, S.; Robinette, P.A.; Carter, A.F.; Higdon, N.S.; Toon, O.B.; Schoeberl, M.R.; Tuck, A.F. Airborne Lidar Observations in the Wintertime Arctic Stratosphere: Polar Stratospheric Clouds. *Geophys. Res. Lett.* **1990**, *17*, 385–388. [CrossRef]
4. Toon, O.B.; Browell, E.V.; Kinne, S.; Jordan, J. An Analysis of Lidar Observations of Polar Stratospheric Clouds. *Geophys. Res. Lett.* **1990**, *17*, 393–396. [CrossRef]
5. Carslaw, K.S.; Luo, B.P.; Clegg, S.L.; Peter, T.; Brimblecombe, P.; Crutzen, P.J. Stratospheric Aerosol Growth and HNO_3 Gas Phase Depletion from Coupled HNO_3 and Water Uptake by Liquid Particles. *Geophys. Res. Lett.* **1994**, *21*, 2479–2482. [CrossRef]
6. Tabazadeh, A.; Turco, R.P.; Drdla, K.; Jacobson, M.Z.; Toon, O.B. A Study of Type I Polar Stratospheric Cloud Formation. *Geophys. Res. Lett.* **1994**, *21*, 1619–1622. [CrossRef]
7. Tritscher, I.; Pitts, M.C.; Poole, L.R.; Alexander, S.P.; Cairo, F.; Chipperfield, M.P.; Grooß, J.-U.; Höpfner, M.; Lambert, A.; Luo, B.; et al. Polar Stratospheric Clouds: Satellite Observations, Processes, and Role in Ozone Depletion. *Rev. Geophys.* **2021**, *59*, e2020RG000702. [CrossRef]
8. Carslaw, K.S.; Wirth, M.; Tsias, A.; Luo, B.P.; Dörnbrack, A.; Leutbecher, M.; Volkert, H.; Renger, W.; Bacmeister, J.T.; Peter, T. Particle Microphysics and Chemistry in Remotely Observed Mountain Polar Stratospheric Clouds. *J. Geophys. Res. Atmos.* **1998**, *103*, 5785–5796. [CrossRef]
9. Wirth, M.; Tsias, A.; Dörnbrack, A.; Weiß, V.; Carslaw, K.S.; Leutbecher, M.; Renger, W.; Volkert, H.; Peter, T. Model-Guided Lagrangian Observation and Simulation of Mountain Polar Stratospheric Clouds. *J. Geophys. Res. Atmos.* **1999**, *104*, 23971–23981. [CrossRef]
10. Lambert, A.; Santee, M.L.; Livesey, N.J. Interannual Variations of Early Winter Antarctic Polar Stratospheric Cloud Formation and Nitric Acid Observed by CALIOP and MLS. *Atmos. Chem. Phys.* **2016**, *16*, 15219–15246. [CrossRef]
11. Ansmann, A.; Ohneiser, K.; Chudnovsky, A.; Knopf, D.A.; Eloranta, E.W.; Villanueva, D.; Seifert, P.; Radenz, M.; Barja, B.; Zamorano, F.; et al. Ozone Depletion in the Arctic and Antarctic Stratosphere Induced by Wildfire Smoke. *Atmos. Chem. Phys.* **2022**, *22*, 11701–11726. [CrossRef]
12. Koop, T.; Ng, H.P.; Molina, L.T.; Molina, M.J. A New Optical Technique to Study Aerosol Phase Transitions: The Nucleation of Ice from H_2SO_4 Aerosols. *J. Phys. Chem. A* **1998**, *102*, 8924–8931. [CrossRef]
13. Engel, I.; Luo, B.P.; Pitts, M.C.; Poole, L.R.; Hoyle, C.R.; Grooß, J.-U.; Dörnbrack, A.; Peter, T. Heterogeneous Formation of Polar Stratospheric Clouds—Part 2: Nucleation of Ice on Synoptic Scales. *Atmos. Chem. Phys.* **2013**, *13*, 10769–10785. [CrossRef]
14. Voigt, C.; Dörnbrack, A.; Wirth, M.; Groß, S.M.; Pitts, M.C.; Poole, L.R.; Baumann, R.; Ehard, B.; Sinnhuber, B.-M.; Woiwode, W.; et al. Widespread Polar Stratospheric Ice Clouds in the 2015–2016 Arctic Winter—Implications for Ice Nucleation. *Atmos. Chem. Phys.* **2018**, *18*, 15623–15641. [CrossRef]

15. Salawitch, R.J.; Wofsy, S.C.; Gottlieb, E.W.; Lait, L.R.; Newman, P.A.; Schoeberl, M.R.; Loewenstein, M.; Podolske, J.R.; Strahan, S.E.; Proffitt, M.H.; et al. Chemical Loss of Ozone in the Arctic Polar Vortex in the Winter of 1991–1992. *Science* **1993**, *261*, 1146–1149. [CrossRef] [PubMed]
16. Hunt, B.G. Photochemistry of Ozone in a Moist Atmosphere. *J. Geophys. Res.* **1966**, *71*, 1385–1398. [CrossRef]
17. Nicolet, M. The Origin of Nitric Oxide in the Terrestrial Atmosphere. *Planet. Space Sci.* **1970**, *18*, 1111–1118. [CrossRef]
18. Spang, R.; Arndt, K.; Dudhia, A.; Höpfner, M.; Hoffmann, L.; Hurley, J.; Grainger, R.G.; Griessbach, S.; Poulsen, C.; Remedios, J.J.; et al. Fast Cloud Parameter Retrievals of MIPAS/Envisat. *Atmos. Chem. Phys.* **2012**, *12*, 7135–7164. [CrossRef]
19. Spang, R.; Hoffmann, L.; Müller, R.; Grooß, J.-U.; Tritscher, I.; Höpfner, M.; Pitts, M.; Orr, A.; Riese, M. A Climatology of Polar Stratospheric Cloud Composition between 2002 and 2012 Based on MIPAS/Envisat Observations. *Atmos. Chem. Phys.* **2018**, *18*, 5089–5113. [CrossRef]
20. Lecours, M.; Bernath, P.; Boone, C.; Crouse, J. Infrared Transmittance Spectra of Polar Stratospheric Clouds. *J. Quant. Spectrosc. Radiat. Transf.* **2023**, *294*, 108406. [CrossRef]
21. Lavy, L.; Bernath, P.; Lecours, M.; English, D.; Fromm, M. Comparison between ACE and CALIPSO Observations of Antarctic Polar Stratospheric Clouds. *J. Quant. Spectrosc. Radiat. Transf.* **2024**, *313*, 108827. [CrossRef]
22. Achtert, P.; Tesche, M. Assessing Lidar-based Classification Schemes for Polar Stratospheric Clouds Based on 16 Years of Measurements at Esrange, Sweden. *J. Geophys. Res. Atmos.* **2014**, *119*, 1386–1405. [CrossRef]
23. Pitts, M.C.; Poole, L.R.; Gonzalez, R. Polar Stratospheric Cloud Climatology Based on CALIPSO Spaceborne Lidar Measurements from 2006 to 2017. *Atmos. Chem. Phys.* **2018**, *18*, 10881–10913. [CrossRef]
24. Achtert, P.; Khosrawi, F.; Blum, U.; Fricke, K.H. Investigation of Polar Stratospheric Clouds in January 2008 by Means of Ground-Based and Spaceborne Lidar Measurements and Microphysical Box Model Simulations. *J. Geophys. Res. Atmos.* **2011**, *116*, D07201. [CrossRef]
25. Achtert, P.; Karlsson Andersson, M.; Khosrawi, F.; Gumbel, J. On the Linkage between Tropospheric and Polar Stratospheric Clouds in the Arctic as Observed by Space–Borne Lidar. *Atmos. Chem. Phys.* **2012**, *12*, 3791–3798. [CrossRef]
26. Zhu, Y.; Toon, O.B.; Pitts, M.C.; Lambert, A.; Bardeen, C.; Kinnison, D.E. Comparing Simulated PSC Optical Properties with CALIPSO Observations during the 2010 Antarctic Winter: Comparing Simulated PSC With CALIPSO. *J. Geophys. Res. Atmos.* **2017**, *122*, 1175–1202. [CrossRef]
27. Zhu, Y.; Toon, O.B.; Lambert, A.; Kinnison, D.E.; Bardeen, C.; Pitts, M.C. Development of a Polar Stratospheric Cloud Model Within the Community Earth System Model: Assessment of 2010 Antarctic Winter. *J. Geophys. Res. Atmos.* **2017**, *122*, 10418–10438. [CrossRef]
28. Tritscher, I.; Grooß, J.-U.; Spang, R.; Pitts, M.C.; Poole, L.R.; Müller, R.; Riese, M. Lagrangian Simulation of Ice Particles and Resulting Dehydration in the Polar Winter Stratosphere. *Atmos. Chem. Phys.* **2019**, *19*, 543–563. [CrossRef]
29. Steiner, M.; Luo, B.; Peter, T.; Pitts, M.C.; Stenke, A. Evaluation of Polar Stratospheric Clouds in the Global Chemistry–Climate Model SOCOLv3.1 by Comparison with CALIPSO Spaceborne Lidar Measurements. *Geosci. Model Dev.* **2021**, *14*, 935–959. [CrossRef]
30. Zhu, Y.; Toon, O.B.; Lambert, A.; Kinnison, D.E.; Brakebusch, M.; Bardeen, C.G.; Mills, M.J.; English, J.M. Development of a Polar Stratospheric Cloud Model within the Community Earth System Model Using Constraints on Type I PSCs from the 2010–2011 Arctic Winter. *J. Adv. Model. Earth Syst.* **2015**, *7*, 551–585. [CrossRef]
31. Hanson, D.R.; Ravishankara, A.R. Reactive Uptake of $ClONO_2$ onto Sulfuric Acid Due to Reaction with HCl and H_2O. *J. Phys. Chem.* **1994**, *98*, 5728–5735. [CrossRef]
32. Wegner, T.; Kinnison, D.E.; Garcia, R.R.; Solomon, S. Simulation of Polar Stratospheric Clouds in the Specified Dynamics Version of the Whole Atmosphere Community Climate Model: POLAR STRATOSPHERIC CLOUDS IN SD-WACCM 4. *J. Geophys. Res. Atmos.* **2013**, *118*, 4991–5002. [CrossRef]
33. Dhomse, S.; Chipperfield, M.P.; Feng, W.; Haigh, J.D. Solar Response in Tropical Stratospheric Ozone: A 3-D Chemical Transport Model Study Using ERA Reanalyses. *Atmos. Chem. Phys.* **2011**, *11*, 12773–12786. [CrossRef]
34. Chipperfield, M.P.; Bekki, S.; Dhomse, S.; Harris, N.R.P.; Hassler, B.; Hossaini, R.; Steinbrecht, W.; Thiéblemont, R.; Weber, M. Detecting Recovery of the Stratospheric Ozone Layer. *Nature* **2017**, *549*, 211–218. [CrossRef]
35. Weber, M.; Arosio, C.; Feng, W.; Dhomse, S.S.; Chipperfield, M.P.; Meier, A.; Burrows, J.P.; Eichmann, K.; Richter, A.; Rozanov, A. The Unusual Stratospheric Arctic Winter 2019/20: Chemical Ozone Loss from Satellite Observations and TOMCAT Chemical Transport Model. *J. Geophys. Res. Atmos.* **2021**, *126*, e2020JD034386. [CrossRef]
36. Chipperfield, M.P.; Dhomse, S.S.; Feng, W.; McKenzie, R.L.; Velders, G.J.M.; Pyle, J.A. Quantifying the Ozone and Ultraviolet Benefits Already Achieved by the Montreal Protocol. *Nat. Commun.* **2015**, *6*, 7233. [CrossRef]
37. Dhomse, S.S.; Feng, W.; Montzka, S.A.; Hossaini, R.; Keeble, J.; Pyle, J.A.; Daniel, J.S.; Chipperfield, M.P. Delay in Recovery of the Antarctic Ozone Hole from Unexpected CFC-11 Emissions. *Nat. Commun.* **2019**, *10*, 5781. [CrossRef] [PubMed]
38. Feng, W.; Chipperfield, M.P.; Davies, S.; von der Gathen, P.; Kyrö, E.; Volk, C.M.; Ulanovsky, A.; Belyaev, G. Large Chemical Ozone Loss in 2004/2005 Arctic Winter/Spring. *Geophys. Res. Lett.* **2007**, *34*, L09803. [CrossRef]
39. Wohltmann, I.; Wegner, T.; Müller, R.; Lehmann, R.; Rex, M.; Manney, G.L.; Santee, M.L.; Bernath, P.; Sumińska-Ebersoldt, O.; Stroh, F.; et al. Uncertainties in Modelling Heterogeneous Chemistry and Arctic Ozone Depletion in the Winter 2009/2010. *Atmos. Chem. Phys.* **2013**, *13*, 3909–3929. [CrossRef]

40. Nakajima, H.; Wohltmann, I.; Wegner, T.; Takeda, M.; Pitts, M.C.; Poole, L.R.; Lehmann, R.; Santee, M.L.; Rex, M. Polar Stratospheric Cloud Evolution and Chlorine Activation Measured by CALIPSO and MLS, and Modeled by ATLAS. *Atmos. Chem. Phys.* **2016**, *16*, 3311–3325. [CrossRef]
41. Feng, W.; Dhomse, S.S.; Arosio, C.; Weber, M.; Burrows, J.P.; Santee, M.L.; Chipperfield, M.P. Arctic Ozone Depletion in 2019/20: Roles of Chemistry, Dynamics and the Montreal Protocol. *Geophys. Res. Lett.* **2021**, *48*, e2020GL091911. [CrossRef]
42. Kuttippurath, J.; Feng, W.; Müller, R.; Kumar, P.; Raj, S.; Gopikrishnan, G.P.; Roy, R. Exceptional Loss in Ozone in the Arctic Winter/Spring of 2019/2020. *Atmos. Chem. Phys.* **2021**, *21*, 14019–14037. [CrossRef]
43. Ardra, D.; Kuttippurath, J.; Roy, R.; Kumar, P.; Raj, S.; Müller, R.; Feng, W. The Unprecedented Ozone Loss in the Arctic Winter and Spring of 2010/2011 and 2019/2020. *ACS Earth Space Chem.* **2022**, *6*, 683–693. [CrossRef]
44. Winker, D.M.; Hunt, W.H.; McGill, M.J. Initial Performance Assessment of CALIOP. *Geophys. Res. Lett.* **2007**, *34*, L19803. [CrossRef]
45. Pitts, M.C.; Thomason, L.W.; Poole, L.R.; Winker, D.M. Characterization of Polar Stratospheric Clouds with Spaceborne Lidar: CALIPSO and the 2006 Antarctic Season. *Atmos. Chem. Phys.* **2007**, *7*, 5207–5228. [CrossRef]
46. Pitts, M.C.; Poole, L.R.; Lambert, A.; Thomason, L.W. An Assessment of CALIOP Polar Stratospheric Cloud Composition Classification. *Atmos. Chem. Phys.* **2013**, *13*, 2975–2988. [CrossRef]
47. Pitts, M.C.; Poole, L.R.; Thomason, L.W. CALIPSO Polar Stratospheric Cloud Observations: Second-Generation Detection Algorithm and Composition Discrimination. *Atmos. Chem. Phys.* **2009**, *9*, 7577–7589. [CrossRef]
48. Gelaro, R.; McCarty, W.; Suárez, M.J.; Todling, R.; Molod, A.; Takacs, L.; Randles, C.A.; Darmenov, A.; Bosilovich, M.G.; Reichle, R.; et al. The Modern-Era Retrospective Analysis for Research and Applications, Version 2 (MERRA-2). *J. Clim.* **2017**, *30*, 5419–5454. [CrossRef]
49. Chipperfield, M.P. New Version of the TOMCAT/SLIMCAT off-Line Chemical Transport Model: Intercomparison of Stratospheric Tracer Experiments. *Q. J. R. Meteor. Soc.* **2006**, *132*, 1179–1203. [CrossRef]
50. Feng, W.; Chipperfield, M.P.; Roscoe, H.K.; Remedios, J.J.; Waterfall, A.M.; Stiller, G.P.; Glatthor, N.; Höpfner, M.; Wang, D.-Y. Three-Dimensional Model Study of the Antarctic Ozone Hole in 2002 and Comparison with 2000. *J. Atmos. Sci.* **2005**, *62*, 822–837. [CrossRef]
51. Zhang, J.; Tian, W.; Xie, F.; Chipperfield, M.P.; Feng, W.; Son, S.-W.; Abraham, N.L.; Archibald, A.T.; Bekki, S.; Butchart, N.; et al. Stratospheric Ozone Loss over the Eurasian Continent Induced by the Polar Vortex Shift. *Nat. Commun.* **2018**, *9*, 206. [CrossRef]
52. Zhang, J.; Zhang, C.; Zhang, K.; Xu, M.; Duan, J.; Chipperfield, M.P.; Feng, W.; Zhao, S.; Xie, F. The Role of Chemical Processes in the Quasi-Biennial Oscillation (QBO) Signal in Stratospheric Ozone. *Atmos. Environ.* **2021**, *244*, 117906. [CrossRef]
53. Snels, M.; Scoccione, A.; Di Liberto, L.; Colao, F.; Pitts, M.; Poole, L.; Deshler, T.; Cairo, F.; Cagnazzo, C.; Fierli, F. Comparison of Antarctic Polar Stratospheric Cloud Observations by Ground-Based and Space-Borne Lidar and Relevance for Chemistry–Climate Models. *Atmos. Chem. Phys.* **2019**, *19*, 955–972. [CrossRef]
54. Hersbach, H.; Bell, B.; Berrisford, P.; Hirahara, S.; Horányi, A.; Muñoz-Sabater, J.; Nicolas, J.; Peubey, C.; Radu, R.; Schepers, D.; et al. The ERA5 Global Reanalysis. *Q. J. R. Meteor. Soc.* **2020**, *146*, 1999–2049. [CrossRef]
55. Feng, W.; Chipperfield, M.P.; Dorf, M.; Pfeilsticker, K.; Ricaud, P. Mid-Latitude Ozone Changes: Studies with a 3-D CTM Forced by ERA-40 Analyses. *Atmos. Chem. Phys.* **2007**, *7*, 2357–2369. [CrossRef]
56. Li, Y.; Dhomse, S.S.; Chipperfield, M.P.; Feng, W.; Chrysanthou, A.; Xia, Y.; Guo, D. Effects of Reanalysis Forcing Fields on Ozone Trends and Age of Air from a Chemical Transport Model. *Atmos. Chem. Phys.* **2022**, *22*, 10635–10656. [CrossRef]
57. Coy, L.; Nash, E.R.; Newman, P.A. Meteorology of the Polar Vortex: Spring 1997. *Geophys. Res. Lett.* **1997**, *24*, 2693–2696. [CrossRef]
58. Lawrence, Z.D.; Manney, G.L.; Wargan, K. Reanalysis Intercomparisons of Stratospheric Polar Processing Diagnostics. *Atmos. Chem. Phys.* **2018**, *18*, 13547–13579. [CrossRef] [PubMed]
59. Ivy, D.J.; Solomon, S.; Kinnison, D.; Mills, M.J.; Schmidt, A.; Neely III, R.R. The Influence of the Calbuco Eruption on the 2015 Antarctic Ozone Hole in a Fully Coupled Chemistry-Climate Model. *Geophys. Res. Lett.* **2017**, *44*, 2556–2561. [CrossRef]
60. Shen, X.; Wang, L.; Osprey, S. The Southern Hemisphere Sudden Stratospheric Warming of September 2019. *Sci. Bull.* **2020**, *65*, 1800–1802. [CrossRef]
61. Manney, G.L.; Lawrence, Z.D. The Major Stratospheric Final Warming in 2016: Dispersal of Vortex Air and Termination of Arctic Chemical Ozone Loss. *Atmos. Chem. Phys.* **2016**, *16*, 15371–15396. [CrossRef]
62. Khosrawi, F.; Kirner, O.; Sinnhuber, B.-M.; Johansson, S.; Höpfner, M.; Santee, M.L.; Froidevaux, L.; Ungermann, J.; Ruhnke, R.; Woiwode, W.; et al. Denitrification, Dehydration and Ozone Loss during the 2015/2016 Arctic Winter. *Atmos. Chem. Phys.* **2017**, *17*, 12893–12910. [CrossRef]
63. Hu, J.; Li, T.; Xu, H. Relationship between the North Pacific Gyre Oscillation and the Onset of Stratospheric Final Warming in the Northern Hemisphere. *Clim. Dyn.* **2018**, *51*, 3061–3075. [CrossRef]
64. Qin, Y.; Gu, S.; Dou, X.; Teng, C.; Li, H. On the Westward Quasi-8-Day Planetary Waves in the Middle Atmosphere During Arctic Sudden Stratospheric Warmings. *J. Geophys. Res. Atmos.* **2021**, *126*, e2021JD035071. [CrossRef]
65. Manney, G.L.; Santee, M.L.; Rex, M.; Livesey, N.J.; Pitts, M.C.; Veefkind, P.; Nash, E.R.; Wohltmann, I.; Lehmann, R.; Froidevaux, L.; et al. Unprecedented Arctic Ozone Loss in 2011. *Nature* **2011**, *478*, 469–475. [CrossRef]
66. Feng, W.; Chipperfield, M.P.; Davies, S.; Mann, G.W.; Carslaw, K.S.; Dhomse, S.; Harvey, L.; Randall, C.; Santee, M.L. Modelling the Effect of Denitrification on Polar Ozone Depletion for Arctic Winter 2004/2005. *Atmos. Chem. Phys.* **2011**, *11*, 6559–6573. [CrossRef]

67. Hoffmann, L.; Spang, R.; Orr, A.; Alexander, M.J.; Holt, L.A.; Stein, O. A Decadal Satellite Record of Gravity Wave Activity in the Lower Stratosphere to Study Polar Stratospheric Cloud Formation. *Atmos. Chem. Phys.* **2017**, *17*, 2901–2920. [CrossRef]
68. Zhang, J.; Tian, W.; Chipperfield, M.P.; Xie, F.; Huang, J. Persistent Shift of the Arctic Polar Vortex towards the Eurasian Continent in Recent Decades. *Nat. Clim. Change* **2016**, *6*, 1094–1099. [CrossRef]
69. Lambert, A.; Santee, M.L.; Wu, D.L.; Chae, J.H. A-Train CALIOP and MLS Observations of Early Winter Antarctic Polar Stratospheric Clouds and Nitric Acid in 2008. *Atmos. Chem. Phys.* **2012**, *12*, 2899–2931. [CrossRef]